



Queensland University of Technology
Brisbane Australia

This is the author's version of a work that was submitted/accepted for publication in the following source:

Chang, Jin & Waclawik, Eric (2012) Facet-controlled Self-assembly of ZnO Nanocrystals by Non-Hydrolytic Aminolysis and their Photodegradation Activities. *CrystEngComm*.

This file was downloaded from: <http://eprints.qut.edu.au/50089/>

© Copyright 2012 Royal Society of Chemistry.

Notice: *Changes introduced as a result of publishing processes such as copy-editing and formatting may not be reflected in this document. For a definitive version of this work, please refer to the published source:*

<http://dx.doi.org/10.1039/c2ce25154j>

Cite this: DOI: 10.1039/c2ce25154j

www.rsc.org/crystengcomm

PAPER

Facet-controlled self-assembly of ZnO nanocrystals by non-hydrolytic aminolysis and their photodegradation activities†

Jin Chang and Eric R. Waclawik*

Received 3rd February 2012, Accepted 18th March 2012

DOI: 10.1039/c2ce25154j

We report a method for controlling the exposed facets and hence the dimensionality and shape of ZnO nanocrystals using a non-hydrolytic aminolysis synthesis route. The effects of changes to reaction conditions on ZnO formation were investigated and possible self-assembly mechanisms proposed. The crystal facet growth and hence morphologies of the ZnO nanocrystals were controlled by varying reaction temperature and the reactant ratio. Four distinct ZnO nanocrystal types were produced (nanocones, nanobullets, nanorods and nanoplates). The relative photocatalytic activities of the exposed facets of these ZnO nanostructures were also examined, which showed the activities obviously depended on the reactivity of exposed crystal facets in the order: {1011} >> {0001}, {1010}.

1. Introduction

Crystalline metal oxides are used as active device components in a wide range of research fields. Frequently the aim of these studies is to exploit nanoscale effects on their optical, electric and magnetic properties for optoelectronic and related applications.¹ To this end, in the last decade, considerable effort has been devoted to the controllable synthesis of nanocrystals with reduced dimensionality and well-defined morphologies because the exposed crystal facets can often determine their properties and activities.^{2–5} Among these materials, zinc oxide nanocrystals have attracted great attention because of their potential application in fields such as solar cells,^{6–8} photocatalysis,⁹ UV laser,¹⁰ chemical sensing^{11–13} and electricity generation^{14–16} from ZnO nanorod arrays. Due to the promising perspectives for ZnO in these areas, a large number of ZnO synthesis techniques have been developed for these purposes. Among these synthesis techniques, wet-chemical methods are of interest since they are very versatile with regards to the controlling of nanocrystal structures, compositions and morphologies.^{17,18} Wet-chemical methods can basically be divided into hydrolytic and non-hydrolytic methods, depending on whether water is involved in the reaction procedure. Conventionally, ZnO nanostructures are prepared by hydrolytic methods using autoclaves (also known as hydrothermal methods) because of factors such as ease of scale-up and convenience. In order to obtain monodisperse samples, surfactants such as sodium dodecyl sulfate are often applied to control the growth and morphologies of ZnO samples.^{19–21} However, surface-adsorbed surfactants can have unpredictable

influences on the passivation, reactivity and the segregation of nanocrystal surface properties, which are critical when it comes to catalysis and gas sensing applications for instance.^{22–25} Non-hydrolytic methods provide a promising alternative approach to preparing nanocrystalline materials. Originally reported by Ebelman²⁶ and Graham,²⁷ non-hydrolytic synthesis studies on silica gel has since been extended to the synthesis of metal oxides, binary metal oxides and multi-metal systems such as perovskites²⁸ and spinels.²⁹ The preparation of ZnO by non-hydrolytic methods was recently reported using the ester elimination reaction between zinc acetate and 1,12-dodecanediol,³⁰ followed by Chin's similar work using alkyl-amine medium.³¹ Meanwhile, benzyl alcohol and other alcohols have also been used to prepare ZnO nanostructures.^{1,32} The “benzyl alcohol route” was further developed for the preparation of other metal oxides and organic–inorganic hybrid nanomaterials.^{33,34} It is important to note that the synthesis protocol for a particular nanomaterial by these methods often involves more than one mechanism, such as a combination of alcoholysis and thermal decomposition of zinc precursors which occurs at high temperature, resulting in incomplete understanding of the mechanism route.

Crystalline materials provided with differently exposed facets are likely to have different properties and activities, useful in a variety of applications. For example, anatase TiO₂ crystals with exposed {001} facets have demonstrated enhanced energy conversion efficiency for dye-sensitized solar cell applications.³⁵ The {111} surfaces of rutile TiO₂ nanocrystals show excellent photocatalytic, antibacterial activity due to providing active OH species under irradiation.³⁶ The photo-degradation activity of α -Fe₂O₃ under visible light has also been shown to be strongly depended on the exposed crystal facets in the order {110} > {012} >> {001}.³⁷ Moreover, ZnO {0001} crystal facets have been found to be more active than {000 $\bar{1}$ } or {10 $\bar{1}$ 0} facets in

Discipline of Chemistry, Queensland University of Technology, 2 George St., Brisbane, (QLD), 4000, Australia. E-mail: e.waclawik@qut.edu.au; Fax: +61 07 3138 1804; Tel: +61 07 3138 2579

† Electronic Supplementary Information (ESI) available. See DOI: 10.1039/c2ce25154j/

both photocatalytic and gas sensing applications.^{9,38,39} The photocatalytic activities of other crystal facets such as ZnO {10 $\bar{1}$ 1} facets have not been reported yet.

In this work, therefore, ZnO nanocrystals with different exposed facets, *i.e.* {10 $\bar{1}$ 1}, {10 $\bar{1}$ 0}, {0001} and {000 $\bar{1}$ } were prepared *via* a non-hydrolytic method. The morphologies and crystal facets of these ZnO nanostructures were controlled by varying the reaction temperature and reactant ratio. The probable formation mechanism is discussed and explained for each ZnO nanocrystal. The influence of different synthetic mechanisms on the growth of ZnO nanocrystals were illustrated by the controllable synthesis of desired morphologies. Finally, the photocatalytic activities of these ZnO nanocrystals were examined and the reactivity of different crystal facets was investigated.

2. Experimental

2.1 Materials

Anhydrous zinc acetate (Zn(OAc)₂, Sigma-Aldrich, 99.99%), benzyl ether ((C₆H₅CH₂)₂O, Sigma-Aldrich, 98%), benzylamine (C₆H₅CH₂NH₂, Sigma-Aldrich, 99%), Rhodamine B ([9-(2-carboxyphenyl)-6-diethylamino-3-xanthenylidene]-diethylammonium chloride or Rh B, Sigma-Aldrich, 95%). All chemicals were used as received without further purification or distillation.

2.2 Sample synthesis

ZnO nanocones. All synthetic procedures were conducted under a nitrogen atmosphere using standard Schlenk techniques. To prepare ZnO nanocones, anhydrous Zn(OAc)₂ (0.183 g, 1 mmol) was added into benzyl ether (10 mL), then the mixture was heated at 170 °C. When zinc acetate was dissolved, benzylamine (1.07 g, 10 mmol) was injected into the solution and heated for a further 24 h. After reaction, the solution was cooled down to room temperature, and the white precipitate was separated by centrifugation. The resulting white powder was washed several times with acetone and dried in a vacuum oven at 90 °C for 12 h.

ZnO nanobullets. Anhydrous Zn(OAc)₂ (0.183 g, 1 mmol) was added into benzyl ether (10 mL) and the mixture was heated at 210 °C for 1 h. Then benzylamine (1.07 g, 10 mmol) was injected into the solution and heated for a further 5 h at the same temperature. After reaction, the solution was cooled down to room temperature, and the white precipitate was separated by centrifugation. The resulting white powder was washed several times with acetone and dried in a vacuum oven at 90 °C for 12 h.

ZnO nanorods. Anhydrous Zn(OAc)₂ (0.183 g, 1 mmol) was added into benzyl ether (10 mL) and the mixture was heated at 210 °C. Then benzylamine (0.107 g, 1 mmol) was injected into the solution and heated for a further 5 h at the same temperature. After reaction, the solution was cooled down to room temperature, and the white precipitate was separated by centrifugation. The resulting white powder was washed several times with acetone and dried in a vacuum oven at 90 °C for 12 h.

ZnO nanoplates. Anhydrous Zn(OAc)₂ (0.183 g, 1 mmol) and benzylamine (4.28 g, 40 mmol) were added into benzyl ether (10 mL). Then the mixture was heated rapidly to 220 °C and refluxed for a further 5 h. After the reaction, the solution was cooled down to room temperature, and the white precipitate was separated by centrifugation. The resulting white powder was washed several times with acetone and dried in a vacuum oven at 90 °C for 12 h.

2.3 Characterization

The structure, morphology and crystalline nature of the samples were characterized by X-ray diffraction spectrometry (XRD, PANalytical XPert Pro Multi Purpose Diffractometer) using Cu-K α radiation (λ = 0.154178 nm), field-emission scanning electron microscopy (FE-SEM, JEOL 7001F), transmission electron microscopy (TEM, JEOL 1010) and high resolution transmission electron microscopy (HR-TEM, JEOL 2100). Electronic absorption spectra were obtained using a UV-vis spectrometer (Varian, Cary 100). FT-IR spectra of as-prepared samples were collected on Perkin-Elmer 1000 with microscope at resolution of 4 cm⁻¹ and 64 scans.

2.4 Photocatalytic activity measurements

The photo-degradation of Rhodamine B dye (Rh B) was used to study the photocatalytic properties of the three ZnO nanocrystals. For each measurement, 0.02 g ZnO powder was added into a glass vial containing 10 mL deionized water. After sonication, 10 mL Rh B dye (1.0×10^{-5} mol L⁻¹) was added into above solution and the mixture was stirred in the dark for 30 min. Then the suspension was stirred and irradiated with a Black Ray UV lamp (365 nm, 100 W, Ultra-Violet Products, Inc.). The samples with different reaction times were taken out and centrifuged for the absorbance measurements. The quantity of Rh B in solution was determined by the absorption intensity at 554 nm, the main absorption peak of Rh B dye.

3. Result and discussion

Four ZnO nanocrystal types were synthesized from anhydrous zinc acetate by non-aqueous, aminolysis using benzylamine (BA). By controlling the reaction conditions carefully and making subtle variations to the synthesis procedure, the synthesis mechanism for each ZnO nanocrystal type could be understood. The first nanostructure was obtained by simply heating zinc acetate and benzylamine in benzyl ether solvent at 170 °C for 24 h. Fig. 1a shows the X-ray diffraction (XRD) pattern of the obtained white powder, which was consistent with that of the wurtzite ZnO crystal structure (*P*6₃mc, *a* = 3.249 Å, *c* = 5.206 Å, JCPDS, 36-1451). Fig. 1b displays the representative field-emission scanning electron microscopy (FE-SEM) image of the ZnO nanocrystals. The transmission electron microscopy (TEM) images (Fig. 1c, d) show that these nanocrystals were well shaped ZnO nanocones with an average size of 100 nm width \times 100 nm height. The inset of Fig. 1c exhibits the side (top-left) and tilted (bottom-left, *X* = 41.1°, *Y* = 0) views of a single ZnO nanocone. The measured angle between the edge and the basal plane of this ZnO nanocone was approximately 58°. Fig. 1d confirms the morphology as hexagonal nanocones, where the top-view of the

nanostructure is marked by red dashes. To investigate the crystalline nature of the ZnO nanocones, the selected area electron diffraction (SAED) pattern of the marked nanocone in Fig. 1d was obtained and shown in Fig. 1e. The pattern shows that the [0001] zone axis of the hexagonal cone was surrounded by $\{10\bar{1}0\}$ planes. From the SAED pattern and the angle between the edge and the basal plane of the hexagonal cones, we identified the exposed six side surfaces as $\{10\bar{1}1\}$ facets. Fig. 1f shows a model of a ZnO hexagonal nanocone with 30% $\{000\bar{1}\}$ facets as base and 70% $\{10\bar{1}1\}$ facets as side surfaces.

Before discussing the formation mechanism of the ZnO nanocone structure, it should be noted that wurtzite ZnO crystals often grow along the [0001] direction with crystal facets of: a top polar zinc (0001) facet, six nonpolar $\{10\bar{1}0\}$ facets parallel to the [0001] direction, and polar oxygen $\{000\bar{1}\}$ plane.⁴⁰ The nonpolar $\{10\bar{1}0\}$ facets are more stable than polar (0001) and $\{000\bar{1}\}$ facets because $\{10\bar{1}0\}$ facets have relative lower surface energies.⁴¹ For ZnO nanocones, however, high-energy $\{10\bar{1}1\}$ facets were exposed instead of the more stable $\{10\bar{1}0\}$ facets. We speculated that crystal termination on the $\{10\bar{1}1\}$ facet could be favoured by applying benzylamine in the reaction system. Here, benzylamine not only acted as reaction agent in the aminolysis of $\text{Zn}(\text{OAc})_2$ process but also as a capping agent to stabilize the $\{10\bar{1}1\}$ planes. Mechanisms previously suggested for formation of ZnO nanostructures in alcohol or amine^{1,30,31} solutions do not apply to the particular set of reaction conditions employed here because those other reaction schemes pertain to thermal decomposition or mixed alcoholysis with aminolysis routes. This makes it difficult to relate the figures of these different reaction mechanisms to the present study. Here, ZnO nanocones were obtained at 170 °C where aminolysis was likely to be the preferred mechanism simply because zinc acetate does not decompose to ZnO at this temperature without benzylamine. Scheme 1 shows the suggested formation mechanism of the ZnO nanocone sample. In the beginning of the reaction, benzylamine is coordinated with Zn^{2+} to form $\text{Zn}(\text{OAc})_2$ -BA complex. Then,

the aminolysis reaction takes place *via* a nucleophilic substitution ($\text{S}_{\text{N}}2$) type mechanism between benzylamine and the acetate group of $\text{Zn}(\text{OAc})_2$, to form zinc hydroxide and *N*-benzylacetamide. Finally, zinc hydroxide was transformed into ZnO through dehydration at the reaction temperature.

To elucidate the proposed mechanism, we recorded the FT-IR spectra of neat $\text{Zn}(\text{OAc})_2$ and benzylamine, $\text{Zn}(\text{OAc})_2$ treated by benzylamine at 100 °C and the separated residue after heating for 24 h at 170 °C. As shown in Fig. 2, the C=O asymmetric stretching vibration of $\text{Zn}(\text{OAc})_2$ at 1555 cm^{-1} red shifted by $\sim 17\text{ cm}^{-1}$ when it was heated with benzylamine at 100 °C. This could be due to the formation of $\text{Zn}(\text{OAc})_2$ -BA complex and the donor NH_2 group sharing its lone-pair of electrons with the Zn^{2+} ions. After heating for 24 h at 170 °C, white ZnO product was separated by centrifugation and the reaction residue exhibited a new peak at 1648 cm^{-1} which was attributed to the stretching vibration of C=O group in amide,⁴² *i.e.* the byproduct shown in Scheme 1.

To investigate the growth process of the nanocone structure, as-prepared samples were removed from the reaction vessel at different reaction times (1 h, 3 h, 8 h and 24 h) for XRD and TEM characterization. The XRD result shows that wurtzite ZnO crystal was formed at the beginning of the reaction (Fig. S1). The peaks were slightly sharper as the reaction time increased, indicating the growth of nanocrystals. As shown in Fig. 3a, in the first 1 h of the reaction, ZnO crystal aggregates quickly formed which were self-assembled from several irregular triangle-shape nanocrystals. In the following hours (3–8 h), ZnO nanocrystals grew further and partially changed into hexagonal cones by the recrystallization of self-assembled nanocrystals (Fig. 3b). Fig. 3c shows a nanocone only partially-created at the 8 h stage of the reaction, indicating ZnO cones grow in the direction from base to top through self-assembly and recrystallization processes.

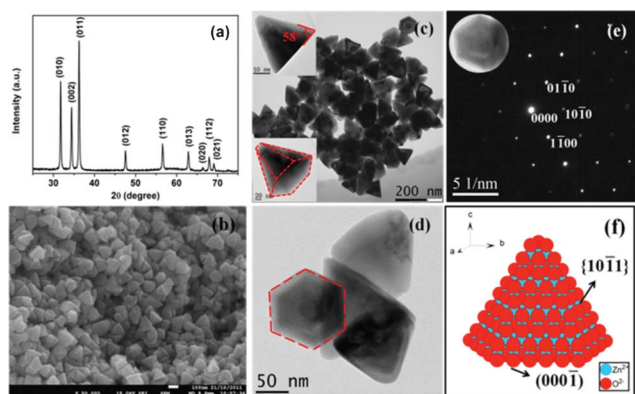


Fig. 1 (a) XRD pattern of the white powder product synthesized from $\text{Zn}(\text{OAc})_2$ and benzylamine at 170 °C in benzylether solution (BA/ Zn^{2+} molar ratio = 10). (b) FE-SEM image of the morphology of the prepared white powder, the scale bar is 100 nm. (c) TEM image of the as-prepared ZnO nanocone product; the insets show the side view of a nanocone (left-top) and the tilted ($X = 41.1^\circ$, $Y = 0$) view of the nanocone (left-bottom). (d) Enlarged TEM image with the top view of a nanocone. (e) SAED pattern of the ZnO nanocone marked in (d). (f) Schematic model of a ZnO hexagonal nanocone.

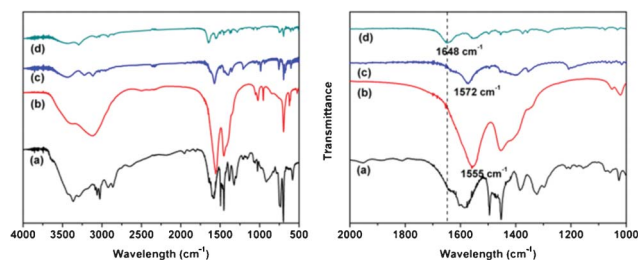
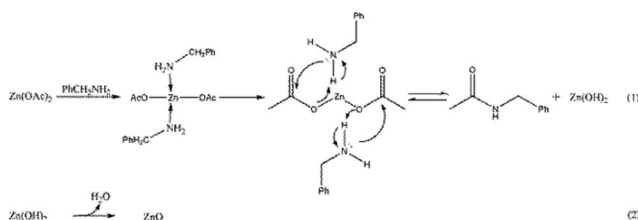


Fig. 2 FT-IR transmission spectra in the full range (left) and magnified scale (right) for (a) benzylamine, (b) $\text{Zn}(\text{OAc})_2$, (c) $\text{Zn}(\text{OAc})_2$ treated by benzylamine at 100 °C and (d) reaction residue after reaction at 170 °C for 24 h.



Scheme 1 Proposed formation mechanism of the ZnO nanocone sample by the reaction between zinc acetate and benzylamine.

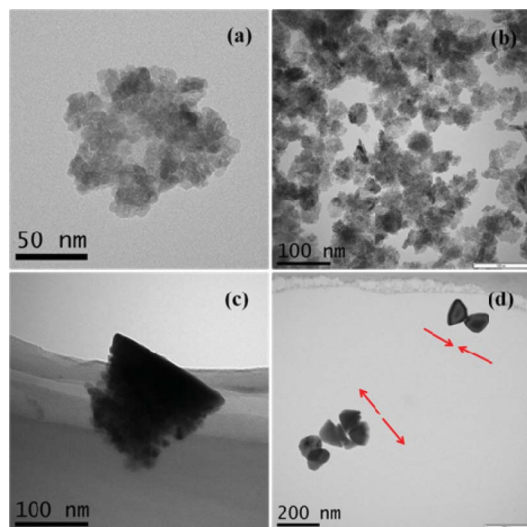


Fig. 3 TEM images of as-prepared ZnO nanocones measured at different reaction stages: (a) 1 h, (b) 3 h, (c) 8 h and (d) 24 h.

After complete growth, the ZnO nanocones were found to be attracted to each other either in a head-to-head or tail-to-tail fashion along the c -axis of [0001] direction (Fig. 3d). Structurally and electronically ZnO nanocrystal colloids are highly anisotropic. Fig. S2 shows the HRTEM image of the final product along the [0001] zone axis with the lattice spacing of 0.28 nm, corresponding to the distance between $\{10\bar{1}0\}$ planes. It is generally accepted that each ZnO nanocrystal possesses a dipole moment (D) along the 0001 axis. In aqueous ZnO systems D tends to reduce as the ZnO crystals assemble and grow.⁴³ Considering the uni-directional nature of the dipole of each ZnO nanocone, the favored self-assembly pattern is likely to be head-to-tail. The un-favored head-to-head and tail-to-tail assembly observed in Fig. 3d could be due to the excluded volume interactions contributed by the benzylamine and benzyl ether. In hydrolytic synthesis of ZnO, side reactions have been demonstrated to have a significant influence on nanocrystal assembly/disassembly.⁴³ Another factor determining formation of the ZnO nanocone structures was the combined effect of benzyl ether/benzylamine solution which controls the self-assembly and recrystallization process. It was found that in the absence of benzylamine, ZnO could not be obtained unless the temperature was increased to 210 °C in benzyl ether. In this case, ZnO was produced by the thermal decomposition of zinc acetate. The morphology of the ZnO product under these conditions is shown in the ESI Fig. S3a,† which was more like nanosheets instead of nanocones. On the other hand, ZnO was readily produced in neat benzylamine at 170 °C or an even lower temperature. However, below 170 °C conditions the morphology was not well-shaped (Fig. S3b). If the solvent benzyl ether was replaced by dimethyl sulfoxide (DMSO), aggregated ZnO nanoparticles were obtained in the presence of benzylamine (Fig. S3c).† These results show that ZnO tends to grow into nanosheets through the thermal decomposition route in the benzyl ether solvent. The ZnO cone morphology was favored in non-polar solvents (such as benzyl ether) instead of polar solvents (such as DMSO). This was because the growth rate of ZnO was much slower in benzyl ether than in DMSO, which was critical to the preparation of

nanostructures with high-energy crystal facets. This explanation is consistent with the fact that a polar aprotic solvent often speeds up the aminolysis reaction operating under a nucleophilic substitution (S_N2) type mechanism.⁴⁴

In addition to the above method, a step-by-step strategy was next applied to the synthesis of alternative ZnO nanostructures. Firstly, $Zn(OAc)_2$ was heated in benzyl ether at 210 °C to form a crystal seed. Then benzylamine (BA/ Zn^{2+} molar ratio = 10) was injected into the solution to conduct the aminolysis reaction between zinc acetate and benzylamine. The obtained powder sample was confirmed as wurtzite ZnO crystal structure ($P6_3mc$, $a = 3.249$ Å, $c = 5.206$ Å, JCPDS, 36-1451) by XRD pattern in Fig. 4a. The representative FE-SEM and TEM images are shown in Fig. 4b and c, respectively. These images show that the morphology of the obtained ZnO sample was a nanobullet structure. The SAED pattern (inset of Fig. 4c) confirmed that these ZnO nanobullets were single-crystalline in nature. Fig. 4d shows the morphology of a typical nanobullet with around 30 nm width and 120 nm length. The cap of the nanobullets possessed a cone structure with dimensions and forms identical to that of ZnO nanocone sample described earlier. The HR-TEM image of the marked edge of the nanobullets given in Fig. 4f reveals these nanobullets were highly crystalline with a lattice spacing of 0.26 nm, corresponding to the distance between (0002) planes in the ZnO crystal lattice. This indicates that the ZnO nanobullets are grown along the c -axis of the [0001] direction, a phenomenon frequently observed for wurtzite-structured materials. Based on the above characterization, a model of the ZnO nanobullet sample is shown in Fig. 4e, exhibiting $\{10\bar{1}0\}$ planes for the six side surfaces and $\{10\bar{1}1\}$ planes for the tip of the bullet.

The formation of ZnO nanobullets involves two synthetic mechanisms (thermal decomposition and aminolysis) within two reaction stages. In the first stage, ZnO crystal seeds were produced by the thermal decomposition of $Zn(OAc)_2$ at high temperature (210 °C). TEM images show that these ZnO nanocrystals self-assembled with plate-like morphologies which

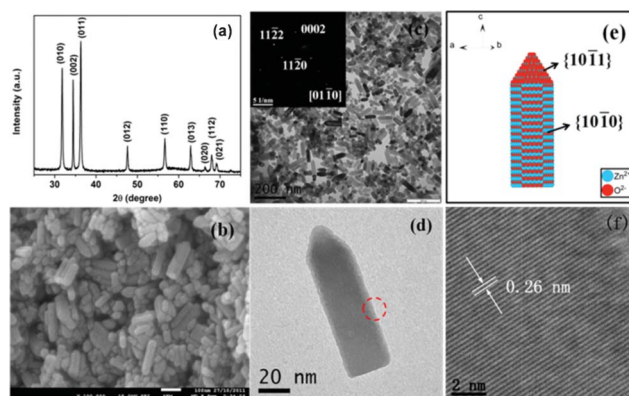


Fig. 4 (a) XRD pattern of the powder synthesized from $Zn(OAc)_2$ in benzyl ether/benzylamine solution through two steps at 210 °C (BA/ Zn^{2+} molar ratio = 10). (b) FE-SEM image of the prepared product, the scale bar is 100 nm. (c) TEM image of the as-prepared ZnO nanobullets and the SAED pattern along the $[01\bar{1}0]$ axis (inset). (d) Enlarged TEM image of an individual nanobullet with 30 nm width and 120 nm length. (e) Schematic model of a ZnO nanobullet. (f) HR-TEM image of the area indicated by the red dash circle in (d).

were composed of hexagonal particles (Fig. S3a). In the second stage, the injection of benzylamine accelerated the nucleation and growth of ZnO crystals through both thermal decomposition and aminolysis routes. It was notable that the final product was bullet-like, indicating the initial hexagonal morphology controls the main morphology. This formation could be due to the higher growth rate of ZnO at 210 °C in the presence of benzylamine. As the reaction proceeded further, the concentration of Zn^{2+} decreased and so to a certain degree the growth rate was likely to slow down so that $\{10\bar{1}1\}$ planes were created in the same way as ZnO nanocones.

To exploit the influence of benzylamine on the ZnO morphology, the BA/ Zn^{2+} molar ratio was reduced from 10 to 1, which was less than the stoichiometric ratio of the aminolysis route. Fig. 5a shows the XRD pattern of the prepared product, which could be indexed as a pure wurtzite ZnO structure (JCPDS No. 36-1451) with calculated lattice constants of $a = 0.3248$ nm and $c = 0.5212$ nm. Fig. 5b–d displays the FE-SEM image and the TEM images of the obtained ZnO sample, exhibiting rounded-ends to the nanorod structure. The SAED pattern obtained and shown in the inset of Fig. 5c confirmed the single crystalline nature of the nanorod material. The HR-TEM image in Fig. 5f showed that the long-edge of the nanorods had a lattice spacing of 0.26 nm, corresponding to the interspacing of the (0002) planes. This indicates that the growth direction of the ZnO nanorods was along $[0001]$ axis, which was the same as that of ZnO nanobullets. Fig. 5e is a schematic model of the ZnO nanorod sample form, where it is clear that a large area or percentage of $\{10\bar{1}0\}$ planes is exposed. By comparing with ZnO nanobullets, it was obvious that the tip of bullets did not form when the BA/ Zn^{2+} ratio was reduced to 1. This indicated excessive benzylamine acted as capping agent in the case of ZnO nanobullets while its main contribution was to accelerate the ZnO growth in the case of ZnO nanorods.

From the above investigation, we understood that the thermal decomposition of $\text{Zn}(\text{OAc})_2$ tended to produce plate-like ZnO in benzyl ether. On the other hand, benzylamine acted as both a reaction reagent and a capping agent in the aminolysis route. To further exploit the effect of the different synthesis routes on ZnO

morphology, we examined a mixture of $\text{Zn}(\text{OAc})_2$, benzylamine (BA/ Zn^{2+} molar ratio = 40) and benzylether, heated rapidly to 220 °C and then kept refluxing for 5 h. After the reaction, a white powder product was obtained and the XRD pattern (Fig. 6a) confirmed it was a pure wurtzite ZnO structure with calculated lattice constants of $a = 0.3249$ nm and $c = 0.5212$ nm. Compared to other XRD peaks, the relative intensity of (002) diffraction peak in this sample was obviously greater than that of ZnO nanocone, nanobullet and nanorod samples, presumably reflecting that the $\{0001\}$ facet was preferentially exposed. Plate-like ZnO nanostructures with around 250 nm width and 40 nm thicknesses were observed in the FE-SEM images of Fig. 6b. Fig. 6c, d displays the TEM images of the obtained ZnO sample, confirming the nanoplate structure. The inset of Fig. 6c shows the SAED pattern of the ZnO nanoplates which confirmed the single crystalline nature of these nanostructures. The HR-TEM image of the area marked in Fig. 6d is shown in Fig. 6f. The HR-TEM image shows 2D lattice fringes with spacing of 0.28 nm, which is in agreement with the interspacing of the $\{10\bar{1}0\}$ planes. These observations identified the 2D plate-like structures formed with $\{0001\}$ surfaces exposed. The corresponding model of the ZnO nanoplate was shown in Fig. 6e.

For these ZnO morphologies, we found that the rapid increase of temperature and the amount of benzylamine were critical for the synthesis of ZnO nanoplates. In this case, the temperature was rapidly increased to 220 °C in 5 min. If the reaction mixture was heated by increasing the temperature slowly (~ 5 °C min^{-1}) and then kept at 220 °C for 5 h, uncompleted ZnO nanocones were obtained instead (Fig. S4).† This suggests that the rapid increase of the temperature favors the formation of ZnO nanoplates, *i.e.* the growth rate along the a , and b axes is faster than the c axis in the thermal decomposition route. Therefore, the obtained ZnO plates were the basal part of the ZnO cones. In addition to temperature control, the BA/ Zn^{2+} ratio also affected the formation of ZnO nanoplates. A large excess of benzylamine (BA/ Zn^{2+} molar ratio = 40) was required for the preparation of ZnO nanoplates. When the ratio was reduced to 10, only ZnO

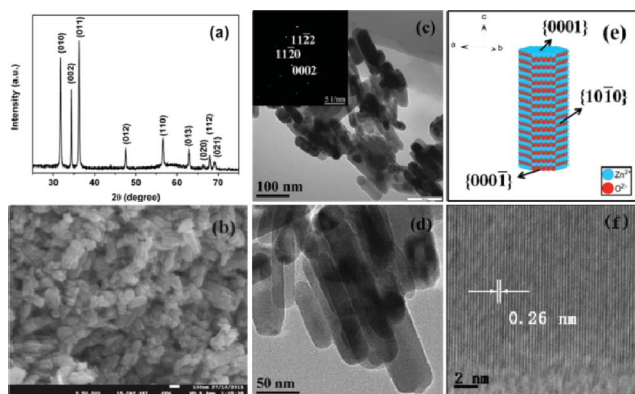


Fig. 5 (a) XRD pattern of the powder synthesized from $\text{Zn}(\text{OAc})_2$ in benzyl ether/benzylamine solution through two steps at 210 °C (BA/ Zn^{2+} molar ratio = 1). (b) FE-SEM image of the prepared sample, the scale bar is 100 nm. (c, d) TEM images of the as-prepared ZnO nanorods and the SAED pattern (inset of c). (e) Schematic model of the ZnO nanorod sample. (f) HR-TEM image of the edge of the ZnO nanorods.

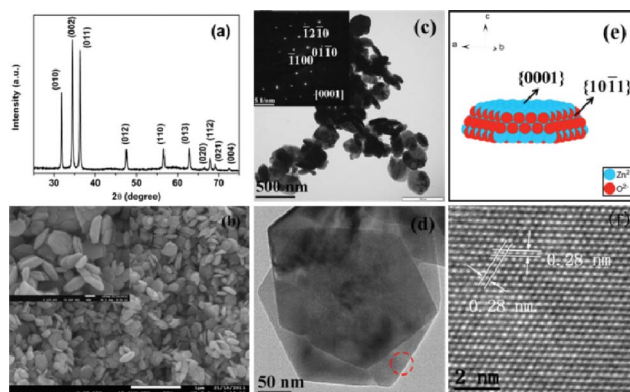


Fig. 6 (a) XRD pattern of the powder synthesized from $\text{Zn}(\text{OAc})_2$ in benzyl ether/benzylamine solution by refluxing at 220 °C (BA/ Zn^{2+} molar ratio = 40). (b) FE-SEM image of the prepared product and an enlarged image (inset), the scale bars are 1 μm and 100 nm, respectively. (c) TEM image of the as-prepared ZnO nanoplates and the SAED pattern along $[0001]$ beam axis (inset). (d) Magnified TEM image of two stacked ZnO nanoplates. (e) Schematic model of the ZnO nanoplates sample. (f) HR-TEM image of the area indicated by the red dash circle in (d).

nanobullets were obtained following the same procedure as the preparation of ZnO nanoplates. This suggests that the extra benzylamine inhibited the growth along the [0001] direction because benzylamine stabilized the polar surface of {0001} planes, probably by coordinating with the Zn^{2+} sites.

The relative photocatalytic activities of the as-prepared ZnO nanostructures were evaluated by measuring the degradation rate of aqueous Rhodamine B solutions in the presence of UV light radiation. The temporal UV-vis spectral changes of Rh B aqueous solutions as a function of irradiation time are shown in Fig. S5. The absorbance of both UV and visible regions decreased with increased UV irradiation time. Fig. 7 shows the normalized concentration (with respect to the optical absorbance measurements at 554 nm) of the Rh B solution containing 20 mg of ZnO catalyst under UV light irradiation (initial concentration of Rh B (C_i): $5.0 \times 10^{-5} \text{ mol L}^{-1}$). In the absence of a catalyst the concentration of the Rh B solution was almost constant during UV irradiation, which confirmed the photostability of the Rh B. It was also demonstrated that ZnO nanocones exhibited the highest photoactivity among the four samples. For comparison, an identical experiment was conducted in the dark and the data is given in Fig. S6.† Compared with the dark reaction, the catalytic activity was dramatically enhanced by the presence of light. To evaluate the photoreactivity quantitatively, the surface area of the different ZnO nanocrystals and the reaction rate constant (k) of Rh B degradation were determined and are summarized in Table 1 and Fig. S5f.† It is shown that the reaction rate was dramatically greatest for ZnO nanocones under UV-light illumination. The reaction rates were relatively smaller and slightly different for the other three ZnO nanostructures in the order of bullets > plates > rods. To explore the intrinsic photoactivity, the reaction rate constant (k) was also normalized to the specific surface area, referred to k_s . Table 1 illustrates that ZnO cones exhibit the greatest photoactivity with $k_s = 32.8 \times 10^{-4} \text{ min}^{-1} \text{ L m}^{-2}$, while k_s is $7.82 \times 10^{-4} \text{ min}^{-1} \text{ L m}^{-2}$, $4.13 \times 10^{-4} \text{ min}^{-1} \text{ L m}^{-2}$ and $2.20 \times 10^{-4} \text{ min}^{-1} \text{ L m}^{-2}$ for nanoplates, nanobullets and nanorods, respectively. Considering

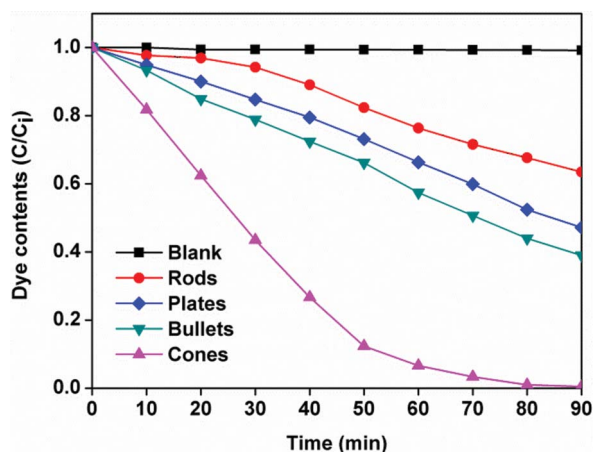


Fig. 7 Photodegradation of Rh B on ZnO nanocrystals with different morphologies under UV irradiation (blank: photo-degradation of Rh B without ZnO samples). Reaction conditions: Rh B concentration $5.0 \times 10^{-5} \text{ mol L}^{-1}$; catalyst concentration 1.0 g L^{-1} ; 100 W UV-Lamp ($\lambda = 365 \text{ nm}$).

the different exposed facets of each nanocrystal, we could conclude that the {10 $\bar{1}$ 1} crystal facets have the highest activity compared with {0001} and {10 $\bar{1}$ 0} facets. Although the normalized reaction rate constant of ZnO plates was slightly higher than that of ZnO bullets, it is difficult to evaluate the relative photoactivities of {0001} and {10 $\bar{1}$ 0} planes in this case, because the {10 $\bar{1}$ 1} crystal plane contributed to photoactivity in both these two samples. Therefore, the relative photoactivities of the ZnO catalyst crystal facets were in the order of {10 $\bar{1}$ 1} >> {0001}, {10 $\bar{1}$ 0}.

It is generally accepted that the reactivity of a metal oxide photocatalyst is determined by the amount of $\cdot\text{OH}$ radicals formed upon UV irradiation.³⁶ Because of their powerful oxidation abilities, $\cdot\text{OH}$ radicals are often regarded as the most important active species for the degradation of organic dyes. Studies have shown that the polar Zn (0001) plane is more reactive than O (000 $\bar{1}$) or nonpolar {10 $\bar{1}$ 0} planes because an abundance of OH^- adheres to the low-coordinate Zn sites of this crystal plane to form highly active $\cdot\text{OH}$ radicals.⁴⁵ However, this suggestion does not completely explain the results obtained here. For the ZnO nanocone sample for instance, the exposed {10 $\bar{1}$ 1} facet was O terminated while it exhibited the highest photoactivity. Fig. 8 depicts atomic models of polar {0001} facets with a Zn and O termination layer, non-polar {10 $\bar{1}$ 0} facet and the {10 $\bar{1}$ 1} facets. It is noted that a {10 $\bar{1}$ 1} facet possesses ridge-and-valley topography with O termination and where the surface O atoms alternate between two-coordinated and three-coordinated sites, while surface Zn and O atoms in other models are all three-coordinated. Since low-coordinated O atoms are generally saturated by H atoms via $\text{O}\cdots\text{H}-\text{O}-\text{H}$ hydrogen bond formations in aqueous solution, we suggested that two-coordinated O atoms are the more active hydrogen bond forming sites which thus produce more $\cdot\text{OH}$ radicals under UV irradiation. This suggestion explains the reason why {10 $\bar{1}$ 1} facets have higher activity than that of {0001} and {10 $\bar{1}$ 0} facets.

We note that recent research has highlighted how the photoreactivity of anatase TiO_2 crystals is not only determined by differences in the coordination of atoms of particular crystal facets, but also by their surface electronic structures.^{47,48} This was clearly demonstrated when the band gap and valence-band maxima of three different facet-exposed TiO_2 crystals were examined by UV-vis absorption and X-ray photoelectron spectra. Cooperative effects of surface atomic coordination and band structure ultimately determined the photoreactivity order of {001}, {101} and {010} facets for TiO_2 nanocrystals. We therefore expect that the photoreactivity of ZnO crystals in this work is likely to be influenced by a contribution from the surface electronic structures as well. In aqueous solution, these factors will combine to determine the relative amounts of $\cdot\text{OH}$ radicals generated at different facets of the ZnO photocatalyst under UV light irradiation.

Conclusions

In summary, we report a method to synthesize facet-controlled ZnO nanocrystals through an aminolysis route in a non-hydrolytic medium. This method allows the control over ZnO nanostructures without the use of surfactant or additives to assist the shaping. The exposed crystal facets of four ZnO nanocrystals

Table 1 Physicochemical properties of ZnO nanocones, nanobullets, nanorods and nanoplates

Sample	Length (nm)	Width (nm)	Height (nm)	SSA ^a (m ² g ⁻¹)	Dominant facets	Reaction rate constants k^b ($\times 10^{-3} \text{ min}^{-1}$)	Normalized rate constants k_s^c ($\times 10^{-4} \text{ min}^{-1} \text{ L m}^{-2}$)
nanorods	100 \pm 20.6	30 \pm 5.3	—	27.4 \pm 3.95	{10 $\bar{1}$ 0}	6.04 \pm 0.26	2.20 \pm 0.49
nanocones	—	250 \pm 20	40 \pm 5	11.8 \pm 1.13	{0001}{10 $\bar{1}$ 1}	9.23 \pm 0.33	7.82 \pm 1.14
nanobullets	120 \pm 15.3	30 \pm 4.1	—	26.9 \pm 3.05	{10 $\bar{1}$ 0}{10 $\bar{1}$ 1}	11.11 \pm 0.49	4.13 \pm 0.73
nanocones	—	100 \pm 15.0	112 \pm 16.8	17.3 \pm 2.24	{0001}{10 $\bar{1}$ 1}	56.70 \pm 1.30	32.8 \pm 5.71

^a The specific surface area (SSA) and dominant facets are determined using TEM. The density of ZnO is 5.606 g cm⁻³ from the Handbook of Chemistry and Physics.⁴⁶ ^b The apparent reaction rate constant (k) of Rh B photodegradation over ZnO is calculated based on a pseudo-first-order kinetic model. ^c k_s denotes the rate constant (k) normalized to SSA, $k_s = k(\text{catalyst concentration} \times \text{SSA})^{-1}$.

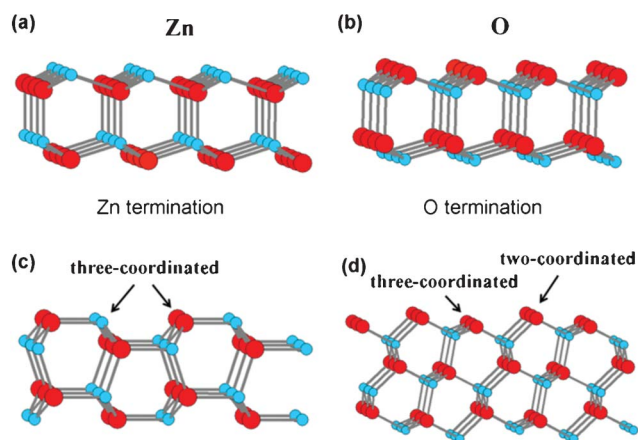


Fig. 8 Side view of surface termination of ZnO: (a,b) {0001} facets with Zn and O termination, respectively; (c) {1010} facet; and (d) {1011} facet. The Zn and O atoms on the {0001} and {1010} surfaces are all three-coordinated while O atoms on the {1011} surface are two-coordinated and three-coordinated.

were simply controlled by varying the reaction temperature and reactant ratio. Based on the experimental results, we proposed likely formation mechanisms for each ZnO nanostructure. The photocatalytic activities of the ZnO nanocrystals were markedly different for the different morphologies, *i.e.*, dependent on the exposed crystal facets. By estimating the surface area of each nanocrystal and the relative reactivity of the crystal facets, we found that {1011} has a much higher photoactivity than {0001} or {10 $\bar{1}$ 0} crystal facets. This was because the surface low-coordinated O atoms are more likely to be saturated by H atoms in aqueous solution, releasing more OH free radical under irradiation, which is a critical species for photocatalysis.

Acknowledgements

Jin wishes to thank the China Scholarship Council (CSC) for providing a scholarship for PhD research. The authors also wish to thank the Queensland Government NIRAP project in Australia for providing the financial support.

References

- X. Zhong, Y. Feng, Y. Zhang, I. Lieberwirth and W. Knoll, *Small*, 2007, **3**, 1194–1199.
- J. Zhang, H. Liu, Z. Wang, N. Ming, Z. Li and A. Biris, *Adv. Funct. Mater.*, 2007, **17**, 3897–3905.

- D. V. Talapin, E. V. Shevchenko, N. Gaponik, I. L. Radtchenko, A. Kornowski, M. Haase, A. L. Rogach and H. Weller, *Adv. Mater.*, 2005, **17**, 1325–1329.
- X. Han, M. Jin, S. Xie, Q. Kuang, Z. Jiang, Y. Jiang, Z. Xie and L. Zheng, *Angew. Chem.*, 2009, **121**, 9344–9347.
- Y. Xia, Y. Xiong, B. Lim and S. E. Skrabalak, *Angew. Chem., Int. Ed.*, 2009, **48**, 60–103.
- X.-F. Wang, O. Kitao, E. Hosono, H. Zhou, S.-i. Sasaki and H. Tamiaki, *J. Photochem. Photobiol., A*, 2010, **210**, 145–152.
- R. Marczak, F. Werner, R. Ahmad, V. Lobaz, D. M. Guldi and W. Peukert, *Langmuir*, 2011, **27**, 3920–3929.
- N. Memarian, I. Concina, A. Braga, S. M. Rozati, A. Vomiero and G. Sberveglieri, *Angew. Chem., Int. Ed.*, 2011, **50**, 12321–12325.
- S. Cho, J.-W. Jang, J. S. Lee and K.-H. Lee, *Langmuir*, 2010, **26**, 14255–14262.
- G. Ouyang and G. W. Yang, *ACS Appl. Mater. Interfaces*, 2012, **4**, 210–213.
- T. T. Trinh, N. H. Tu, H. H. Le, K. Y. Ryu, K. B. Le, K. Pillai and J. Yi, *Sens. Actuators, B*, 2011, **152**, 73–81.
- X. H. Liu, J. Zhang, L. W. Wang, T. L. Yang, X. Z. Guo, S. H. Wu and S. R. Wang, *J. Mater. Chem.*, 2011, **21**, 349–356.
- M. Chen, Z. Wang, D. Han, F. Gu and G. Guo, *Sens. Actuators, B*, 2011, **157**, 565–574.
- M. Riaz, J. Song, O. Nur, Z. L. Wang and M. Willander, *Adv. Funct. Mater.*, 2011, **21**, 628–633.
- M.-Y. Lu, J. Song, M.-P. Lu, C.-Y. Lee, L.-J. Chen and Z. L. Wang, *ACS Nano*, 2009, **3**, 357–362.
- G. Zhu, R. Yang, S. Wang and Z. L. Wang, *Nano Lett.*, 2010, **10**, 3151–3155.
- B. L. Cushing, V. L. Kolesnichenko and C. J. O'Connor, *Chem. Rev.*, 2004, **104**, 3893–3946.
- N. Pinna and M. Niederberger, *Angew. Chem., Int. Ed.*, 2008, **47**, 5292–5304.
- Y. Ni, G. Wu, X. Zhang, X. Cao, G. Hu, A. Tao, Z. Yang and X. Wei, *Mater. Res. Bull.*, 2008, **43**, 2919–2928.
- S. Baruah and J. Dutta, *Sci. Technol. Adv. Mater.*, 2009, **10**, 013001.
- A. Dev, S. K. Panda, S. Kar, S. Chakrabarti and S. Chaudhuri, *J. Phys. Chem. B*, 2006, **110**, 14266–14272.
- M. Baek, M. K. Kim, H. J. Cho, J. A. Lee, J. Yu, H. E. Chung and S. J. Choi, *J. Phys.: Conf. Ser.*, 2011, **304**, 012044.
- R. Y. Hong, J. H. Li, L. L. Chen, D. Q. Liu, H. Z. Li, Y. Zheng and J. Ding, *Powder Technol.*, 2009, **189**, 426–432.
- T. D. Zaveri, N. V. Dolgova, B. H. Chu, J. Y. Lee, J. E. Wong, T. P. Lele, F. Ren and B. G. Keselowsky, *Biomaterials*, 2010, **31**, 2999–3007.
- H. Yin, P. S. Casey, M. J. McCall and M. Fenech, *Langmuir*, 2010, **26**, 15399–15408.
- M. Ebelmen, *Ann. Chim. Phys.*, 1846, **16**, 129–166.
- T. Graham, *J. Chem. Soc.*, 1864, **17**, 318–327.
- P. M. Rørvik, T. Grande and M.-A. Einarsrud, *Adv. Mater.*, 2011, **23**, 4007–4034.
- N. Bao, L. Shen, W. An, P. Padhan, C. Heath Turner and A. Gupta, *Chem. Mater.*, 2009, **21**, 3458–3468.
- J. Joo, S. Kwon, J. Yu and T. Hyeon, *Adv. Mater.*, 2005, **17**, 1873–1877.
- Z. Zhang, M. Lu, H. Xu and W.-S. Chin, *Chem.–Eur. J.*, 2007, **13**, 632–638.
- M. Niederberger and N. Pinna, Springer, UK, 2009.
- N. Pinna, *J. Mater. Chem.*, 2007, **17**, 2769–2774.

- 34 N. Pinna, G. Garnweitner, P. Beato, M. Niederberger and M. Antonietti, *Small*, 2005, **1**, 112–121.
- 35 X. Wu, Z. Chen, G. Q. Lu and L. Wang, *Adv. Funct. Mater.*, 2011, **21**, 4167–4172.
- 36 L. Sun, Y. Qin, Q. Cao, B. Hu, Z. Huang, L. Ye and X. Tang, *Chem. Commun.*, 2011, **47**, 12628–12630.
- 37 X. Zhou, J. Lan, G. Liu, K. Deng, Y. Yang, G. Nie, J. Yu and L. Zhi, *Angew. Chem., Int. Ed.*, 2012, **51**, 178–182.
- 38 J. Liu, X. Chen, W. Wang, Y. Liu, Q. Huang and Z. Guo, *CrystEngComm*, 2011, **13**, 3425–3431.
- 39 J. H. Zeng, B. B. Jin and Y. F. Wang, *Chem. Phys. Lett.*, 2009, **472**, 90–95.
- 40 L. Xu, Y. Guo, Q. Liao, J. Zhang and D. Xu, *J. Phys. Chem. B*, 2005, **109**, 13519–13522.
- 41 B. Meyer and D. Marx, *Phys. Rev. B: Condens. Matter*, 2003, **67**, 035403.
- 42 *The Sadtler Handbook of Infrared Spectra*, Philadelphia, Sadtler Research Laboratories, 1978.
- 43 M. Yang, K. Sun and N. A. Kotov, *J. Am. Chem. Soc.*, 2010, **132**, 1860–1872.
- 44 S. S. Shaik, *J. Am. Chem. Soc.*, 1984, **106**, 1227–1232.
- 45 J. H. Zeng, B. B. Jin and Y. F. Wang, *Chem. Phys. Lett.*, 2009, **472**, 90–95.
- 46 *The CRC Handbook of Chemistry and Physics*, 90th edn, CRC Press, 2009.
- 47 J. Pan, G. Liu, G. Q. Lu and H.-M. Cheng, *Angew. Chem., Int. Ed.*, 2011, **50**, 2133–2137.
- 48 G. Liu, J. C. Yu, G. Q. Lu and H.-M. Cheng, *Chem. Commun.*, 2011, 47.